Magnetic damping in sputter-deposited Co_2MnGe Heusler compounds with $A2$, $B2$, and $L2_1$ orders: Experiment and theory

Justin M. Shaw,[1,*] Erna K. Delczeg-Czirjak,[2] Eric R. J. Edwards,[1] Yaroslav Kvashnin,[2] Danny Thonig,[2]
Martin A. W. Schoen,[1,†] Matt Pufall,[1] Michael L. Schneider,[1] Thomas J. Silva,[1] Olof Karis,[2] Katherine P. Rice,[3]
Olle Eriksson,[2,4] and Hans T. Nembach[1]

[1]*Quantum Electromagnetics Division, National Institute of Standards and Technology, Boulder, Colorado 80305, USA*
[2]*Department of Physics and Astronomy, University Uppsala, S-75120 Uppsala, Sweden*
[3]*CAMECA Instruments, Madison, Wisconsin 53711, USA*
[4]*School of Science and Technology, Örebro University, SE-701 82 Örebro, Sweden*

We show that very low values of the magnetic damping parameter can be achieved in sputter deposited polycrystalline films of Co_2MnGe annealed at relatively low temperatures ranging from 240 °C to 400 °C. Damping values as low as 0.0014 are obtained with an intrinsic value of 0.0010 after spin-pumping contributions are considered. Of importance to most applications is the low value of inhomogeneous linewidth that yields measured linewidths of 1.8 and 5.1 mT at 10 and 40 GHz, respectively. The damping parameter monotonically decreases as the $B2$ order of the films increases. This trend is reproduced and explained by *ab initio* calculations of the electronic structure and damping parameter. Here, the damping parameter is calculated as the structure evolves from $A2$ to $B2$ to $L2_1$ orders. The largest decrease in the damping parameter occurs during the $A2$ to $B2$ transition as the half-metallic phase becomes established.

I. INTRODUCTION

Interest in spin based devices has accelerated in recent years due to the potential to overcome scaling and energy consumption limitations in many computation and data storage technologies. This is because the use of spin currents can reduce or eliminate charge currents, which can lead to considerable reduction of power densities by reducing Ohmic losses [1]. In addition, ferromagnetic materials exhibit hysteresis, which makes them intrinsically suited for memory or data storage applications. However, to switch a magnetic material without the use of external magnetic fields, phenomena such as spin torque or spin-orbit torque must be exploited. The efficiency and speed at which devices based on these phenomena operate is also dependent on other magnetic properties such as the magnetic damping parameter and the efficient generation of spin currents [2,3]. In addition, some magnonic device concepts propose the use of spin excitations as the sole carrier of information, requiring new materials with ultralow damping [4–8]. The potential of such technologies has re-established the need to improve our understanding of magnetic damping as well as seek new materials with low values of the damping parameter. While there have been significant advances in producing high-quality thin-film magnetic insulators with ultralow damping, many applications will require conducting materials [9–11].

One class of material that currently shows promise for spintronic and magnonic applications is Heusler compounds. Of importance is the fact that many of these compounds are half-metallic, meaning that one of the spin bands has a band gap at the Fermi energy (i.e., insulating) while the other spin band is metallic in nature (i.e., conducting). As a result, these materials can theoretically produce 100% polarized spin currents at low temperature [12–18]. This property leads to highly efficient generation of spin currents and large values of giant magnetoresistance, even at room temperature [19,20]. In addition, many half-metallic Heusler compounds are expected to have exceptionally low values of the damping parameter. The formation of a band gap in one of the spin channels generally reduces the total density of states (DOS) at the Fermi energy, resulting in a reduced damping parameter relative to metals. In addition, many of the spin scattering channels—such as spin-flip scattering—are forbidden leading to a further reduction of the damping [21]. This effect is explicitly expressed in a damping term that is suggested to be proportional to the product of the spin-up and spin-down projected DOS at the Fermi level [22]. As a result, several half-metallic Heusler compounds have a predicted damping parameter that can be as low as ≈ 0.0001 [21,23]. While such values have yet to be realized experimentally, there has been significant progress as several groups have reported a measured damping parameter within the range of 0.0007 to 0.0017 [16,24–30].

As a result of all of these characteristics, Heusler compounds have been pursued for applications in spintronics, spin-torque oscillators [31–33], magnetic memory [34], magnonics [35], read heads [36,37], and magnetic sensors. However, fabrication of Heusler compounds can be challenging. Heusler compounds generally require high-temperature growth, high-temperature annealing, and/or epitaxial growth via molecular beam epitaxy to form the half-metallic phase. This requirement severely limits the usability of many Heusler compounds in

---

*Corresponding author: justin.shaw@nist.gov
†Present address: Department of Physics, University of Regensburg, Germany.

many practical technologies where neither growth on a single crystalline substrate nor high-temperature processing is possible. These points can be demonstrated in the application of on-chip spin-transfer torque magnetic random-access memory (STT-RAM) where the memory elements are fabricated at the "back end" on top of the CMOS where registration with the single crystalline substrate has been lost. In addition, the thermal budget must be strictly controlled to prevent interdiffusion of device structures. One material that overcomes this limitation is Co_2MnGe (CMG) where high-quality, polycrystalline CMG can be produced at relatively low temperature [37].

In this work, we show that exceptionally low values of the damping parameter and linewidth can be achieved with sputter-deposited CMG processes at relatively low temperature. The damping parameter correlates with the crystalline order of the compound. Comparison with calculations shows that this variation of the damping parameter is related to the formation of the band gap in the minority spin channel. Of equal importance is the quantitative agreement between the calculated and experimental damping parameter as the crystalline order is varied.

II. EXPERIMENT

A. Sample fabrication and characterization

All samples were co-sputtered at room-temperature (RT) using a stoichiometric Co_2Mn target and a pure Ge target with an Ar pressure of approximately 66 mPa (0.5 mTorr) in a chamber with a base pressure of $\approx 1 \times 10^{-7}$ Pa(1×10^{-9} Torr). A 5-nm Ta seed layer and a 5-nm Ta capping layer were used to provide adhesion to the substrate and to protect the CMG layer from oxidation [Fig. 1(b)]. X-ray reflectometry (XRR) was used to calibrate deposition rates and determine

FIG. 1. (a) X-ray diffraction 2θ scans showing the emergence of the (220) and (400) peaks after being annealed at 240 °C and higher. (b) Schematic cross-section diagram of sample structure. (c) Temperature-dependent VSM magnetometry curve showing the irreversible increase in the magnetization at 240 °C due to crystallization. (d) Example of the magnetic moment vs thickness measured at 300 and 5 K. The *x* intercept indicates the magnetic dead layer thickness.

the resulting physical film thickness. The relative content of Ge was varied by adjusting the power on the Ge source. We found that a slightly Ge-rich stoichiometry of 27% Ge yielded better quality CMG, consistent with previous reports [37]. Other Ge concentrations were studied to optimize our process, but we will only discuss and analyze samples with a nominal 27% Ge content in this work. Atom probe tomography (APT) was used to verify the stoichiometry that yielded a measured composition of Co(2.14 ± 0.05) Mn (0.91 ± 0.02) Ge (0.95 ± 0.02). These data show that the deposited films are also slightly Co rich, indicating that there was some Mn depletion when sputtering from the stoichiometric Co_2Mn target.

X-ray diffraction (XRD) revealed that the CMG layer is quasiamorphous in the as-deposited state, given by the absence of any discernable diffraction peaks in the spectrum as demonstrated by the black data in Fig. 1(a). Samples were *ex situ* annealed for 1 h at a pressure of approximately 1×10^{-4} Pa (1×10^{-6} Torr) to induce crystallization of the CMG layer. The effect of annealing can be seen in Figure 1(c), which shows temperature-dependent vibrating sample magnetometry (VSM) data for a 16-nm sample. An increase in temperature from the as-deposited state to approximately 220 °C shows little change in the magnetic moment of the sample except for the gradual decrease expected from the Bloch $T^{3/2}$ law. However, at 240 °C, there is a large and irreversible increase in the magnetic moment saturating at approximately 300 °C. A further increase in temperature causes a mostly reversible decrease in the moment that is again consistent with the Bloch $T^{3/2}$ law. The reversibility of the magnetic moment above 300 °C was verified when the temperature was ramped back to RT from 400 °C.

The large and irreversible change in magnetic moment at approximately 240 °C originates from crystallization of the CMG layer. In-plane x-ray diffraction spectra [Fig. 1(a)] taken after a 1 h *ex situ* anneal show the presence of diffraction (220) and (004) peaks at 240 °C, which become more intense at 300 °C. (For the sake of simplicity, the diffraction peaks are always indexed according to the ideal $L2_1$ crystalline phase.) The intensities of the peaks do not change significantly above 300 °C (not shown). While not systematically studied, the ordering temperature increases for thinner CMG and can be as high as 280 °C for the thinnest 4-nm layers that we studied.

The structure was further characterized by x-ray diffraction and the lattice constants were determined in both the in-plane and out-of-plane directions. Any experimental offsets to the scattering angle 2θ were corrected using a polycrystalline silicon reference sample. Figure 2 shows the in-plane and out-of-plane lattice constants as a function of the annealing temperature. These data show a significant tetragonal distortion that increases with annealing temperature. However, previous calculations show that such distortions should not affect the half-metallicity of CMG [38]. A two-dimensional (2D) diffraction measurement [tilt angle Ψ versus scattering angle (2θ-ω)] was used to further verify crystalline structure and texture, an example of which is shown in Fig. 3(a). The high intensity peaks are consistent with $A2$, $B2$, and $L2_1$ order. Figure 3(a) shows that all crystallized samples exhibit a [001] strong texture given by the location of the (220) and (400) peaks with respect Ψ, the tilt angle relative to the sample normal.

FIG. 2. The in-plane (black circles) and out-of-plane (blue diamonds) lattice constants as a function of annealing temperature indicating a tetragonal strain that increases with annealing temperature.

To refine the phase identification (i.e., distinguish between $A2$, $B2$, and $L2_1$ phases), the presence or absence of low-intensity (002) and (311) peaks must also be considered. The absence of these peaks indicates an $A2$ crystalline phase, while the presence of the (002) peak is expected for both $B2$ and $L2_1$ order. However, the (311) peak will only be present with $L2_1$ order. Spectra taken for all the samples in this study show the presence of the (002), indicating the presence of at least some $B2$ or $L2_1$ order. However, no (311) peaks appeared in any of

the samples below 20 nm in thickness showing no evidence of $L2_1$ order. This is not the case for much thicker samples. Included in Fig. 3(b) is a spectrum taken from an 80-nm-thick sample, which clearly shows the presence of the (311) peak and thus, $L2_1$ order. We are unsure why the $L2_1$ phase is suppressed at smaller thickness, but we speculate that it could be due to strain and/or the influence of the interfacial region with Ta. It should be noted that the considered peaks may also be present with the $D0_3$ phase, but we exclude the $D0_3$ phase based on the magnetic damping data.

In the absence of $L2_1$ order, the amount of $B2$ order is proportional to the ratio of the normalized intensities of the (002) peak to that of the (004) peak. Quantification of the $B2$ order is complicated by the polycrystalline nature, film thickness, and crystalline texture. As a result, we can report only a relative amount of $B2$ order. Example spectra taken of these peaks in the in-plane geometry are shown in Fig. 3(c). The ratio of the integrated areas of the (002) and (004) peaks are plotted in Fig. 3(d) for both the in-plane and out-of-plane data. The ratio for the out-of-plane data is approximately twice that for the in-plane data. This reduced ratio for the in-plane data is likely a measurement artifact from the low scattering angle of the (002) peak in the grazing incidence geometry. Figure 3(d) shows that as the annealing temperature is increased, the amount of B2 order also increases given by the increase in the ratio of the (002) to (004) peaks.

The presence of a magnetically dead layer was determined from the thickness dependence of magnetic moment obtained
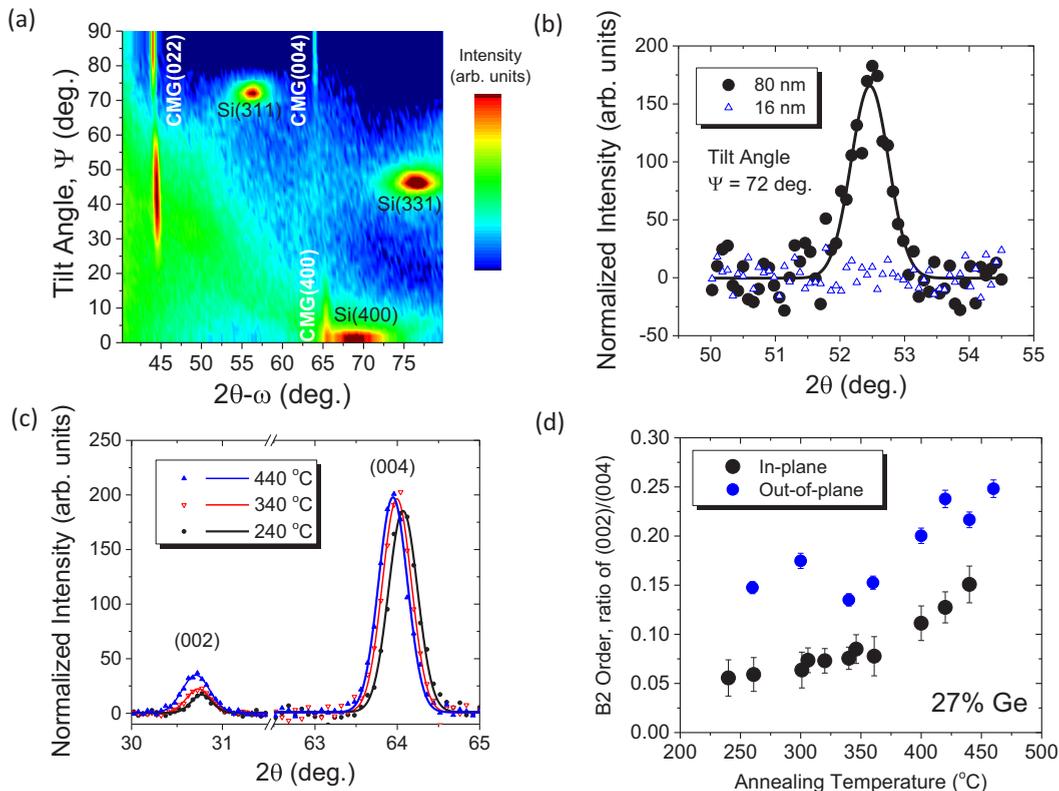
FIG. 3. (a) The [100] texture was confirmed by 2D scans whereby 2θ-ω scans are taken at different tilt angles. (b) A plot of the 2θ-ω scan in the vicinity of the (311) peak. The presence of this peak indicates $L2_1$ order, which is seen only in thicker samples. (c) 2θ-ω scans showing the (002) and (004) peaks at different annealing temperatures. (d) The ratio of the peaks is proportional to amount of $B2$ order, which increases with annealing temperature.

from superconducting quantum interference device (SQUID) magnetometry as shown in Fig. 1(d). The *x* intercept indicates that there is a total dead layer of 1.0 nm in these samples, which was independent of the annealing temperature. Based on the symmetric structure, we assume a dead layer of approximately 0.5 nm at each interface. This is a reasonable value within the context of previously determined values of the dead layer thickness for other ferromagnetic materials in contact with Ta [39–41].

B. Ferromagnetic resonance

The dynamic properties were measured with a broadband vector network analyzer ferromagnetic resonance (VNA-FMR) spectrometer capable of measuring up to 70 GHz frequencies in magnetic fields up to 3 T. Samples were placed face-down on a coplanar waveguide (CPW) and the transmission parameter S21 was measured as the magnetic field was swept through resonance. For all samples with a thickness greater than 5 nm, a 70-μm-thick sapphire spacer was placed between the sample and the waveguide to minimize the radiative contributions to the damping [42]. Measurements were performed with the magnetic field applied perpendicular to sample surface; the so-called perpendicular geometry. This geometry is advantageous in determining the damping parameter since contributions of two-magnon scattering to the linewidth are minimized or excluded [43–46]. Figure 4(a) shows an example of the real and imaginary components of S21 as the field is swept through the resonance. Both the real and imaginary data are simultaneously fit to the Polder susceptibility as detailed in Ref. [47]. From these fits, values of the resonance field and the linewidth were determined for each frequency. Fits to the frequency dependence of the resonance field yield values of the effective magnetization $M_{\text{eff}}(= M_s - H_k)$ and the spectroscopic *g* factor via Eq. (1):

$$f(H_{\text{res}}) = \frac{g\mu_0\mu_B}{2\pi\hbar}(H_{\text{res}} - M_{\text{eff}}), \tag{1}$$

where H_{res} is the resonance field, f is the frequency, μ_B is the Bohr magneton, μ_0 is the permeability of free space, H_k is the perpendicular anisotropy field, and $\hbar$ is the reduced Planck's constant. Values for M_{eff} and the *g* factor were further refined by application of the asymptotic analysis described in Ref [48]. In-plane magnetometry data show no measurable in-plane anisotropy, which is not surprising given the fact that the samples are rotated during growth. Therefore in-plane anisotropy terms were neglected in our analysis.

Figure 4(b) is a plot of the linewidth versus frequency for several 16 nm films annealed at different temperatures. The damping parameter α is determined by fits to Eq. (2),

$$\Delta H(f) = \frac{4\pi\alpha}{|\gamma|\mu_0} + \Delta H_0, \tag{2}$$

where ΔH is the linewidth, $\gamma = (g\mu_B)/\hbar$ is the gyromagnetic ratio, and ΔH_0 is the inhomogeneous contribution to the linewidth [49–51]. As Fig. 4(b) shows, the linewidth data are highly linear for frequencies greater than 10 GHz. However, most samples exhibited some low-field loss effects below this frequency and therefore we only performed measurements and analysis above 10–15 GHz to exclude such contributions that can result in erroneous measurements of the damping

(a)

(b)
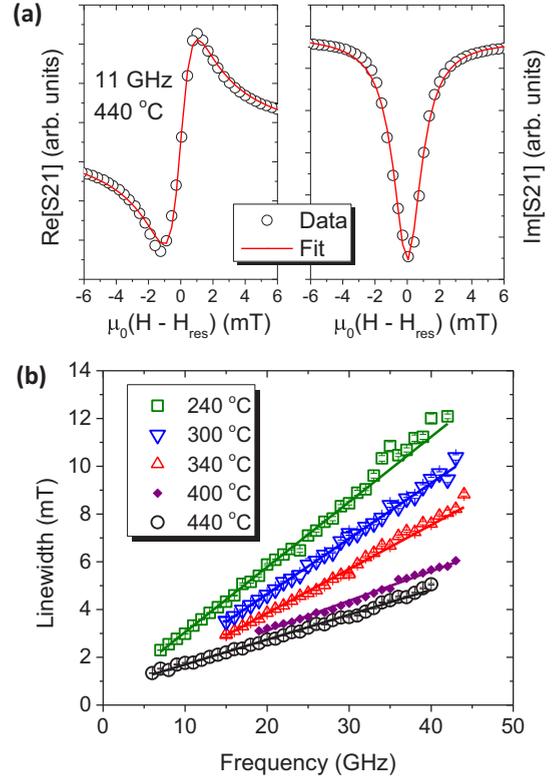
FIG. 4. (a) An example of the real (left) and imaginary (right) transmission signal S21 as the field is swept through the resonance. Fits of the data to the Polder susceptibility tensor are included as the line through the data. (b) Linewidth vs frequency plots used to determine the damping parameter for several 16-nm samples annealed at different temperatures. The error bars are from the fits to the Polder susceptibility.

parameter [52]. In contrast to our previous work, we did not find evidence of a slow-relaxer damping mechanism [47]. We speculate that this is due to the use of different seed and capping layers as well as different processing parameters. Such a damping mechanism was thought to originate from point defects and impurities such as Ge occupying Mn or Co sites. Thus, it would be expected that different growth conditions and stoichiometry will determine the presence and magnitude of any slow-relaxer mechanism.

C. *Ab initio* theory

Electronic structure calculations were performed within the density functional theory framework for different ordering of Co$_2$MnGe. Co$_2$MnGe is a full-Heusler alloy characterized by the X_2YZ formula and the *Fm-3m* (225) crystallographic phase group in its most ordered $L2_1$ cubic phase. In this phase, atoms *X*, *Y*, and *Z* occupy the 8c, 4a, and 4b Wyckoff positions, respectively. The ordering level can be described by the formula

$$\left[\text{Co}_x\text{Mn}_{\frac{1-x}{2}}\text{Ge}_{\frac{1-x}{2}}\right]_2^X \left[\text{Mn}_{0.5-\frac{1-x}{2}+y}\text{Co}_{1-x}\text{Ge}_{0.5-\frac{1-x}{2}-y}\right]^Y$$

$$\times \left[\text{Ge}_{0.5-\frac{1-x}{2}+y}\text{Co}_{1-x}\text{Mn}_{0.5-\frac{1-x}{2}-y}\right]^Z, \tag{3}$$

where X, Y, and Z correspond to the atomic sites described above, and x and y quantify the level of ordering for $A2$ to $B2$ and $B2$ to $L2_1$ transitions, respectively. Each phase can be described by an (x, y) doublet. The completely disordered phase $A2$ is described by the $(x,y) = (0.5,0)$ doublet. The $B2$ phase corresponds to the compound where Co occupies the 8c (X) position while Mn and Ge are equally distributed between the 4a (Y) and 4b (Z) positions, and are described by $(x,y) = (1,0)$. For the fully ordered $L2_1$ cubic phase, described above, the $(1, 0.5)$ doublet pertains.

The disordered phases intermediate between the $A2$ and $B2$ ordering are described by $(x, y = 0)$ with $0.5 \leqslant x \leqslant 1$. In this path, the $(0.5, 0)$ doublet corresponds to the $A2$ phase, meaning that no $B2$ phase is present, whereas the $(1, 0)$ doublet is associated with the $B2$ phase, i.e., 100% $B2$. The variation path between $B2$ and $L2_1$ ordering is described by $(x = 1, y)$ with $0 \leqslant y \leqslant 0.5$. In this path the $(1, 0)$ doublet describes the phase where no $L2_1$ is present, whereas the $(1, 0.5)$ doublet is 100% $L2_1$. For simplicity, the amount (in percent) of $B2$ phase along the $A2$ to $B2$ path and the amount of $L2_1$ phase along the $B2$ to $L2_1$ path will be used to describe the ordering when the results are presented and discussed.

The Kohn-Sham equations are solved as implemented in the spin-polarized relativistic Korringa-Kohn-Rostoker (SPR-KKR) code [53,54]. The chemical disorder was treated within the coherent potential approximation (CPA) [55,56]. We used the Vosko-Wilk-Nusair version of the local spin density approximation for the exchange-correlation functional [57]. The shape of the potential was considered by using both the atomic sphere approximation (ASA) solving the full relativistic Dirac equation and the full potential (FP) scheme combined with scalar relativistic approximation. We sample the irreducible wedge of the Brillouin zone with 1500 k points for the self-consistent cycle, 16000 for the DOS calculations and 1500000 k vectors to calculate the damping parameter, where k is the reciprocal spacer index. For all calculations s, p, d, f orbitals have been included in the basis set ($l_{max} = 3$). All parameters were calculated for the cubic Heusler structure at the experimental lattice parameter of Co$_2$MnGe, which is 0.5814 nm. Neither the experimentally determined tetragonal distortion, variation in lattice parameter, nor the 2% Ge excess has a significant effect on the estimated parameters (data not shown).

The DOS for selected ordering of Co$_2$MnGe was calculated with both the ASA and FP scheme and is shown for the $A2$ structure in Fig. 5(a). The presence of both majority ($\uparrow$) and minority ($\downarrow$) states at the Fermi energy indicate that the $A2$ order is strictly metallic. Included in Figs. 5(a)–5(c) are the calculated density of states (DOS) for structures with partial and full $B2$ order during the $A2 \rightarrow B2$ transition. During this transition, both a decrease in the DOS is observed as well as the formation of a band gap in the minority band. The half-metallic phase is defined by the presence of a band gap in the minority band at the Fermi energy for the $B2$ ordered case [Fig. 5(c)]. Figures 5(d)–5(f) shows additional DOS plots as the order is further improved from the $B2$ phase to the $L2_1$ phase. Within the FP approximation, half metallicity is maintained for all degrees of order during the $B2 \rightarrow L2_1$ transition. This is not the case with the less reliable ASA calculations that show loss of the half-metallic state at intermediate values of
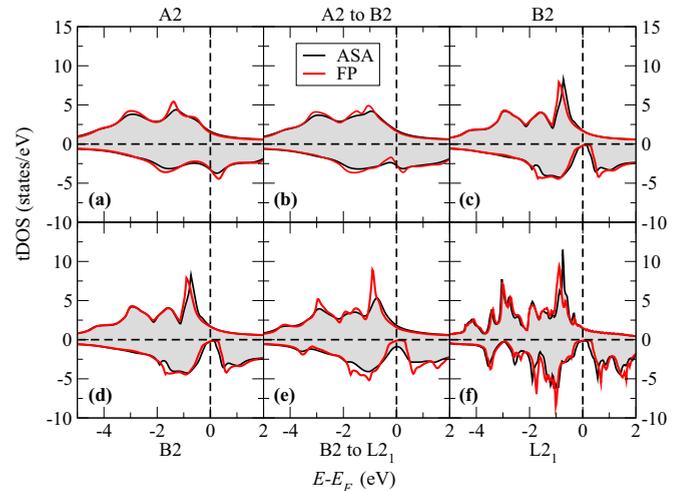
FIG. 5. The total density of states (tDOS) calculated at 0 K for selected ordering of Co$_2$MnGe. Black lines and grey shaded areas correspond to DOS calculated within the ASA scheme, red lines stand for FP calculations. (a) is the tDOS for $A2$; panel (b) the intermediate phase along the $A2 \rightarrow B2$ transition with 52% $B2$ ordering [$x = 0.76$, $y = 0$, see Eq. (3) and the corresponding text]; (c) and (d) correspond to tDOS for B2 phase. (e) is the tDOS for the intermediate phase between $B2$ and $L2_1$ phases [60% $L2_1$ ordering, $x = 1$, $y = 0.3$, see Eq. (3) and the corresponding text]. (f) is the tDOS for $L2_1$ phase with the corresponding $(x = 1, y = 0.5)$ doublet.

order. The comparison between the FP and ASA calculations demonstrate that the particular method used to calculate the DOS can significantly affect the results, in particular when it comes to properties that depend delicately on the details of the electronic structure around the Fermi level.

The damping parameter α at 300 K was calculated via the linear response theory [58]. An alloy analogy model within CPA was considered in order to take into account the temperature effects in the scattering process of electrons with respect to the atomic displacement [59]. The "scattering-in" term of the Boltzmann equations was taken into account via vertex corrections [54,60]. The spectral broadening parameter Γ is extracted from self-consistent Bloch spectral function calculations and was determined to be approximately 0.02–0.03 eV at 300 K for $L2_1$ order. This value suggests that, most likely, the interband scattering contributions are dominant. This is in line with the fact that Γ will increase with disorder which will lead to an increase of damping.

III. RESULTS

A. g factor and orbital moment

Figure 6(a) shows a plot of the g factor as a function of the annealing temperature for CMG of different thickness. All samples show a general trend: immediately after crystallization (240 °C–280 °C), values of the g factor are scattered within a range of approximately 2.05 to 2.06. As the annealing temperature is increased, the g factor gradually decreases to values approaching 2.04. Given that the g factor is defined by the ratio of the orbital moment μ_L to spin moment μ_S as $(g - 2)/2 = \mu_L/\mu_S$, this suggests that the orbital moment
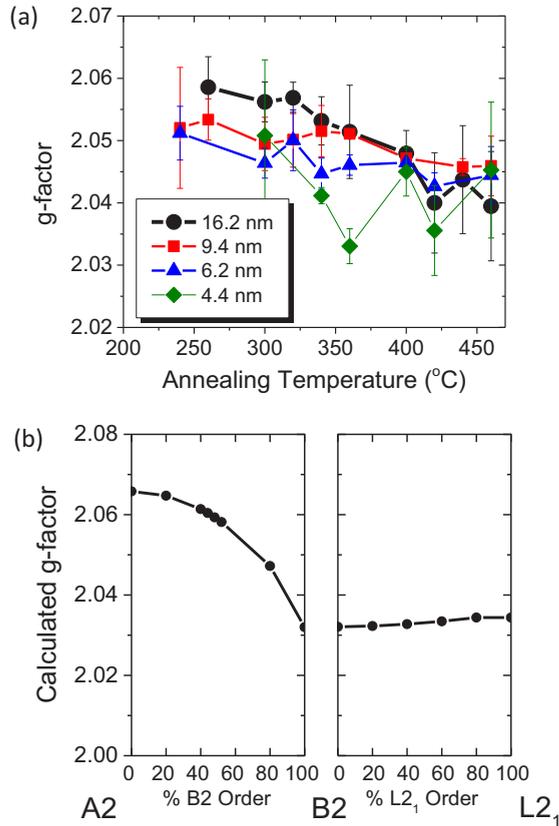
FIG. 6. (a) Measured spectroscopic *g* factor vs the annealing temperature. (b) The calculated *g* factors as the crystalline order evolves from $A2$ (left) to $B2$ (center) to $L2_1$ (right).

decreases with $B2$ order. The spin and orbital moments (and therefore the *g* factor) are also calculated from the DFT calculations, which are given in Table I for the cases of $A2$, $B2$, and $L2_1$ order.

Figure 6(b) shows a plot of the calculated *g* factors as the structure goes from $A2$ (left)$\rightarrow B2$ (center)$\rightarrow L2_1$ (right). These calculations show that the *g* factor for $A2$ order is approximately 2.065 and decreases to 2.03 for $B2$ order. The majority of this change occurs between 50% and 100% $B2$ order. Very little change in the *g* factor occurs as $L2_1$ order becomes established which is consistent with previous calculations for $L2_1$ ordered CMG [61]. These calculations are consistent with our experimental data since an increase in the $B2$ order reduces the *g* factor to an experimental value approaching 2.04. This value is slightly higher than that obtained from calculations for perfect $B2$ order. However, it would take only a small amount of disorder ($\approx 90\% B2$ order) to increase the calculated value of the *g* factor to match experiment.

B. Saturation magnetization and spin moment

Figure 7(a) shows a plot of the saturation magnetization M_s as a function of the annealing temperature obtained from SQUID magnetometry. Immediately after crystallization at 240 °C, $\mu_0 M_s$ for the 16 nm film is approximately 1.15 T and monotonically reduces to 1.0 T as the annealing temperature increases. This suggests that B2 ordered CMG has a lower

spin moment relative to $A2$ order CMG. Indeed, values of M_s calculated from the DFT calculations show a reduction of M_s as the $B2$ order is increased from that of the $A2$ order [Fig. 7(d)]. The elemental spin and orbital moments are listed in Table I and show that the moment on the Co sites decreases by approximately 0.6 μ_B during the $A2 \rightarrow B2$ transition while the moment on the Mn sites increases by approximately 0.6 μ_B. However, because there are two Co atoms for every Mn atom, there is a net reduction in the total moment during this transition. The calculations show no significant change in M_s as the crystalline order evolves from $B2$ to $L2_1$. The calculated values for $L2_1$ order are consistent with previous calculations [61].

The absolute values of the calculated saturation magnetization are approximately 10% higher than those determined experimentally. However, experimentally determined values of M_s have been reported to be consistently lower than those calculated for CMG [18,47,62]. One factor may reside in the fact that our films are nominally 27% Ge (i.e., Ge-rich). In addition, APT indicated that the resulting films are also slightly Co-rich. The elemental spin moments of Co, Mn, and Ge were calculated to be 0.92 μ_B, 3.16 μ_B and -0.08 μ_B, respectively, for stoichiometric $B2$ ordered CMG, consistent with the respective values of 0.7 μ_B and 3.4 μ_B for Co and Mn obtained from x-ray magnetic circular dichroism measurements [63]. As a result, and especially since Ge is predicted to have a negative moment, an excess of Ge and Co will dilute the total magnetic moment of the material since Mn has a significantly higher positive moment relative to both Ge and Co. Such dilution effects can explicitly be seen in the reduction of M_s with increasing Ge content as previously reported in Ref. [47]. Indeed, Table I shows that the calculated total spin moment of CMG when the concentration of Ge is 27% has a reduced total spin moment, despite the fact that there is little change of the elemental moments. The value for $L2_1$ order is within a few percent of the calculations reported by Galanakis [64].

C. Perpendicular anisotropy

In contrast to the saturation magnetization, the effective magnetization M_{eff} shows the opposite trend; increasing as the $B2$ order improves [Fig. 7(a)]. This can be explained by an increase of the perpendicular anisotropy. In this case, the sign of the net perpendicular anisotropy is *negative*, favoring an in-plane magnetization. This picture is further complicated by the fact that the thinner CMG samples exhibit a reduced value of M_{eff}, as shown in Fig. 7(b). This thickness dependence is consistent with the presence of a significant *interfacial* perpendicular anisotropy that is *positive* in sign, favoring an out-of-plane magnetization. These contributions can be quantified by the inverse thickness dependence of the anisotropy energy density $K = \mu_0(M_{eff} - M_s)M_s/2$, which is shown for the case of the 400 °C annealed samples in Fig. 7(c). The *y* intercept is the bulk anisotropy energy density K^{bulk} and the slope is equal to the interfacial anisotropy energy density K^{int}. The factor of 2 arises from the fact that there are two interfaces. The 400 °C annealed samples result in values of $K_{bulk} = -(1.52 \pm 0.02) \times 10^5$ J/m^3 and $K^{int} = (1.95 \pm 0.07) \times 10^{-4}$ J/m^2. Both of these values are substantial in amplitude but, since they are of opposite sign,

TABLE I. Calculated magnetic moments.

	Spin moment/site (μ_B)			Orbital moment/site (μ_B)			Total moment/cell (μ_B)		
25% Ge	A2	B2	L2$_1$	A2	B2	L2$_1$	A2	B2	L2$_1$
Co	1.5266	0.9290	0.9420	0.08295	0.02971	0.03093			
Mn	2.5428	3.1560	3.1341	0.01670	0.01843	0.02244			
Ge	−0.0547	−0.0759	−0.0802	−0.00033	0.00119	0.00060			
							5.5412	4.9382	4.9378
27% Ge	A2	B2	L2$_1$	A2	B2	L2$_1$	A2	B2	L2$_1$
Co	1.4998	0.9226	0.9379	0.08234	0.03019	0.03117			
Mn	2.5508	3.1809	3.1503	0.01698	0.01832	0.02191			
Ge	−0.0520	−0.0684	−0.0610	−0.00022	0.00131	0.00187			
							5.2902	4.6977	4.6943

they mostly compensate for each other within the thickness range that we investigate, which leads to only a modest deviation of M_{eff} from M_s.

D. Damping

Figure 8(a) shows the damping parameter as a function of the annealing temperature. The 16.2-nm-thick CMG layer (black circles) exhibits a damping parameter of $\approx$0.0040 immediately after crystallization at 240 °C. Upon increasing the annealing temperature, the damping parameter decreases until it becomes approximately constant at a value of $\approx$0.0015 at 400 °C. The values of the damping parameter for the thinner CMG layers are higher due to increased spin-pumping contributions from the seed and capping layers. An important observation is the fact that the 4.4-nm and 6.2-nm samples exhibit a minimum of the damping parameter at 360 °C and 400 °C, respectively, versus remaining constant as for the thicker samples. This trend, along with the magnetization data, suggests that the chemical and magnetic properties of
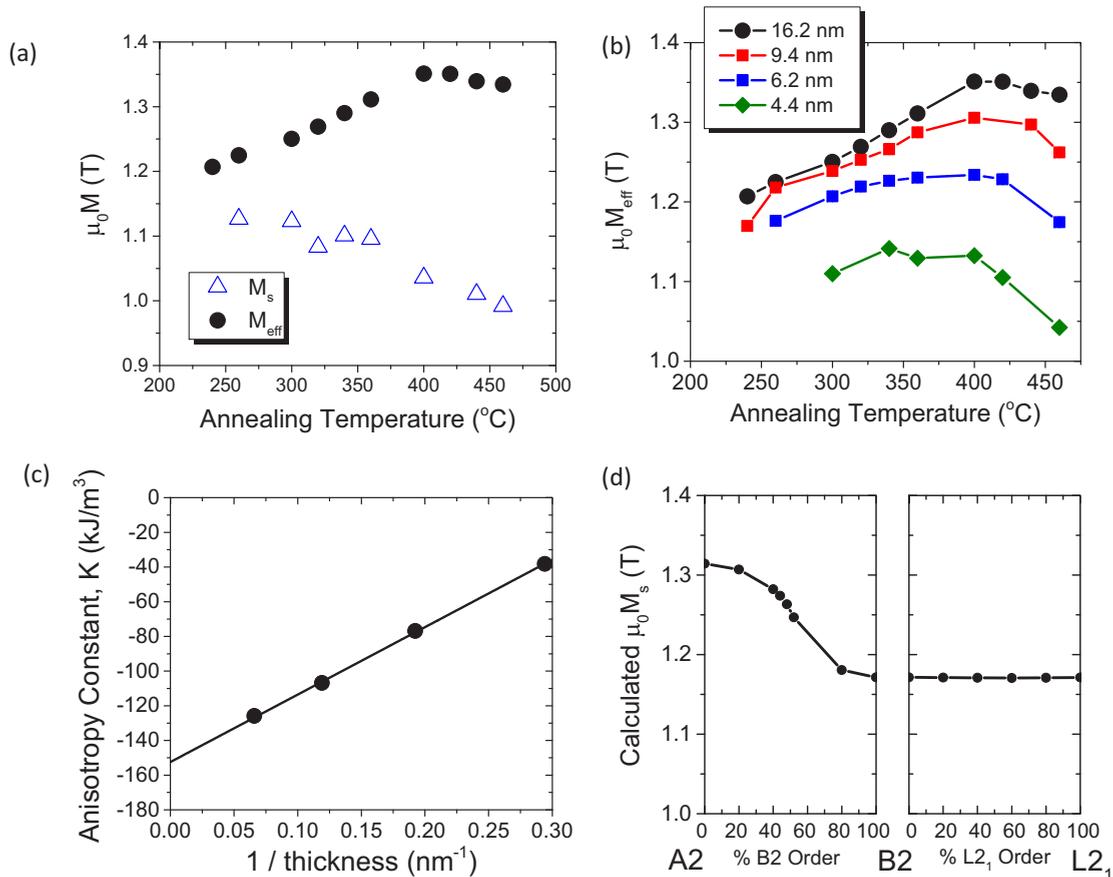
FIG. 7. (a) Measured saturation magnetization (black circles) and effective magnetization (blue triangles) vs the annealing temperature for the 16-nm samples. (b) Measured effective magnetization vs annealing temperature for samples with various thickness. (c) Anisotropy energy density vs the reciprocal thickness for the 400 °C annealed samples used to determine the bulk and interfacial components of the anisotropy. (d) Calculated saturation magnetization as the crystalline order evolves from $A2$ (left) to $B2$ (center) to $L2_1$ (right).
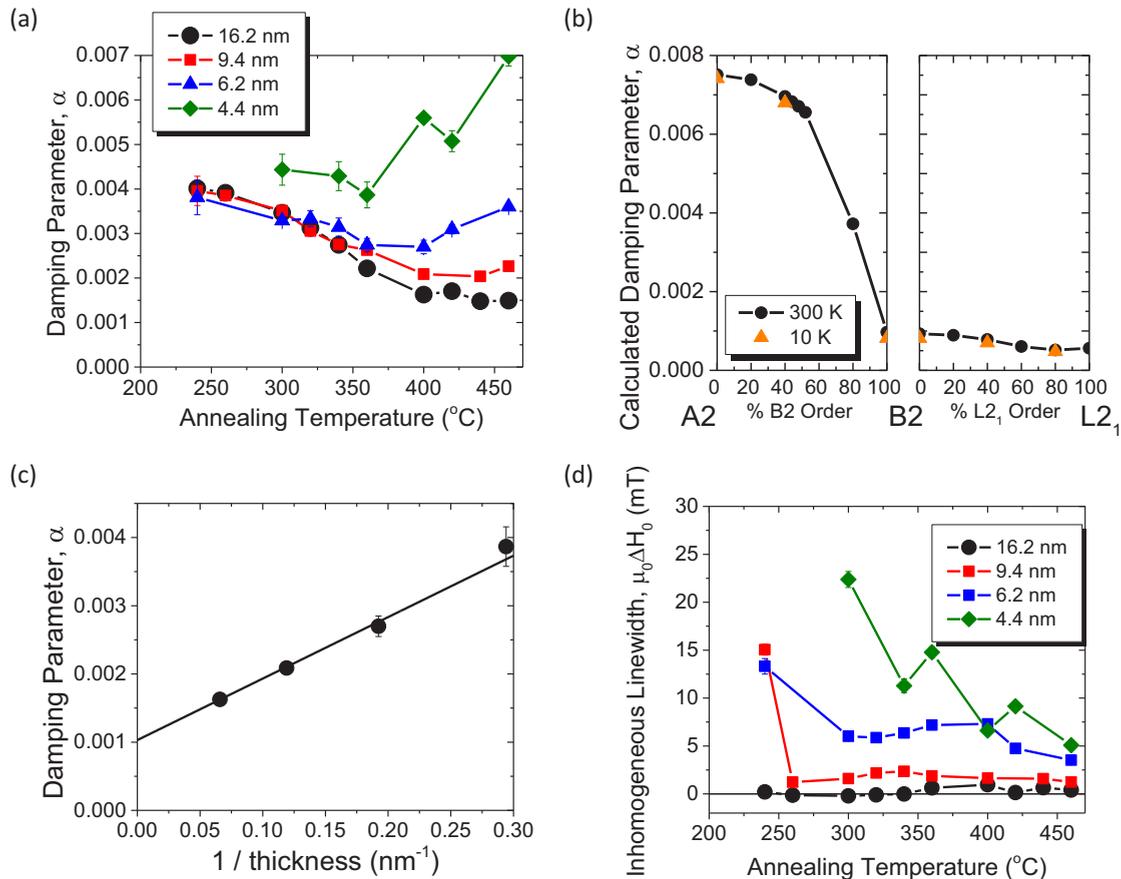
FIG. 8. (a) Measured damping parameter vs annealing temperature for samples with various thickness. (b) Calculated damping parameter at 300 (black) and 10 K (orange) as the crystalline order evolves from $A2$ (left) to $B2$ (center) to $L2_1$ (right). (c) Plot of the damping parameter vs the reciprocal thickness used to account for the spin-pumping contribution to the damping. The y intercept corresponded to the intrinsic damping parameter. (d) Plot of the measured inhomogeneous linewidth vs annealing temperature for samples with various thickness.

the layers degrade above these temperatures in the thinner samples.

Since spin-pumping can phenomenologically be treated as an interfacial contribution to the damping, its presence can be confirmed by plotting the damping parameter versus the inverse thickness as shown in Fig. 8(c) for samples annealed at 400 °C except for the 4.4-nm sample where the minimum damping was used. The y intercept of such a plot is the damping parameter without spin-pumping contributions. Since all other extrinsic contributions to the damping have been minimized, the y intercept also provides a measurement of the intrinsic damping of the material, which is 0.00103 ± 0.00004 for CMG with the highest degree of $B2$ order. This value is in reasonable quantitative agreement with the theoretically calculated value of 0.0009 that we obtained from our DFT calculations [Fig. 8(b)].

Similar to the spin moment and g-factor trends, Fig. 8(b) shows that the calculated damping parameter decreases from 0.0075 to 0.0009 as the $B2$ order increases. The most dramatic decrease occurs between $\approx 60\%$ and 100% B2 order when both the band gap in the minority band forms and the DOS decreases with increased order. This is consistent with the experimental data that show the decrease of the damping parameter from 0.0040 to 0.0015 as the annealing temperature (and $B2$ order) increases for the 16.2-nm samples. (Comparison with the

16.2-nm samples is emphasized since these samples have minimal spin-pumping contribution relative to the thinner samples.) Further ordering from the $B2$ to the $L2_1$ phase has only a small additional reduction of the damping parameter to 0.0005 for 100% $L2_1$ ordered CMG. Previously calculated values of the damping parameter for $L2_1$ ordered CMG have ranged from 0.0002 to 0.0005 [21,23]. The additional ordering has only a small effect on the damping parameter since the half-metallic state was already established in the $B2$ phase and there is only a modest reduction of the DOS as the $L2_1$ order forms.

Finally, the inhomogeneous contribution to the linewidth ΔH_0 is plotted versus the annealing temperature in Fig. 8(d). The thickest 16-nm samples exhibit almost negligible inhomogeneous linewidth broadening. However, ΔH_0 generally increases as the sample thickness is reduced. There is also a general trend where ΔH_0 decreases as the annealing temperature increases. This could be a result of the fact that at low temperature the structure is a mix of $A2$ and $B2$ order, which becomes predominately $B2$ ordered at higher temperatures, thus reducing the structural inhomogeneity.

IV. DISCUSSION

Despite the presence of disorder from the polycrystalline microstructure, as well as the lack of evidence for any $L2_1$
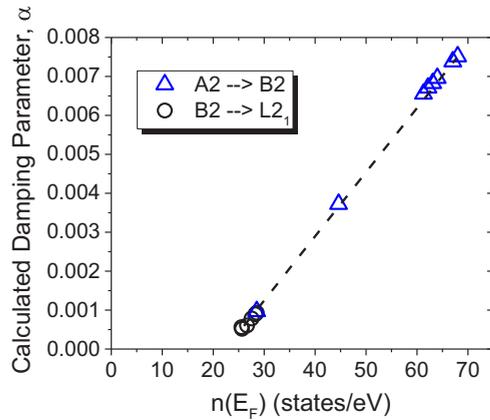
FIG. 9. Calculated damping parameter vs the density of states at the Fermi energy.

crystalline order, an exceptionally low value of 0.0010 is achieved for the intrinsic damping parameter. It is important to stress the limited processing requirements for these CMG films: RT sputter deposition with an anneal at or below 400 °C. From a technological standpoint, this is an important quality of CMG since epitaxial growth and high-temperature annealing would be prohibitive for many applications in spintronics where such materials are needed in "back-end" processes.

We also show that the total damping in 16-nm films can be tuned between approximately 0.0040 and 0.0015. Based on a comparison with our DFT calculations, we conclude that this tuning of the damping is achieved by the reduction of the DOS at the Fermi energy $n(E_F)$ as well as the formation of a minority band gap during the $A2 \rightarrow B2$ crystalline transition. Within the model originally proposed by Kambersky, $n(E_F)$ enters directly into the governing equations for both intraband ("breathing" Fermi surface) and interband ("bubbling" Fermi surface) [65–72]. Within this model, $n(E_F)$ should exhibit a proportionality to the damping—everything else being equal. Indeed, as Fig. 9 shows, our calculations show a proportionality of $n(E_F)$ with the calculated damping. This relationship was also shown in calculations by Chico *et al.* [23] for various Heusler compounds.

Such a relationship between the $n(E_F)$ and α has been experimentally obtained in Co_xFe_{1-x} [73], CoFeGe [74], $Fe_2(Cr,Co)Si$ [30], and Co_2FeAl [24] systems. In the case of half-metals, a further reduction of the damping is expected because the number of spin-scattering channels is reduced. For example, as we show in Fig. 4, a band gap forms at the Fermi energy in the minority spin band. As a result, the absence of any minority spin states at the Fermi energy excludes spin flip or scattering between two minority spins. This effect manifests itself as a dramatic decrease in the damping parameter as the band gap forms in the minority band after the $B2$ order becomes established and very little change in the damping occurs during the $B2 \rightarrow L2_1$ transition. In other words, the band gap is already established with $B2$ order, so the additional order obtained with the $L2_1$ phase only subtly changes $n(E_F)$. Recently, Pradines *et al.* studied the variation of the damping parameter across various ordered and partially disordered phases of Co_2MnSi
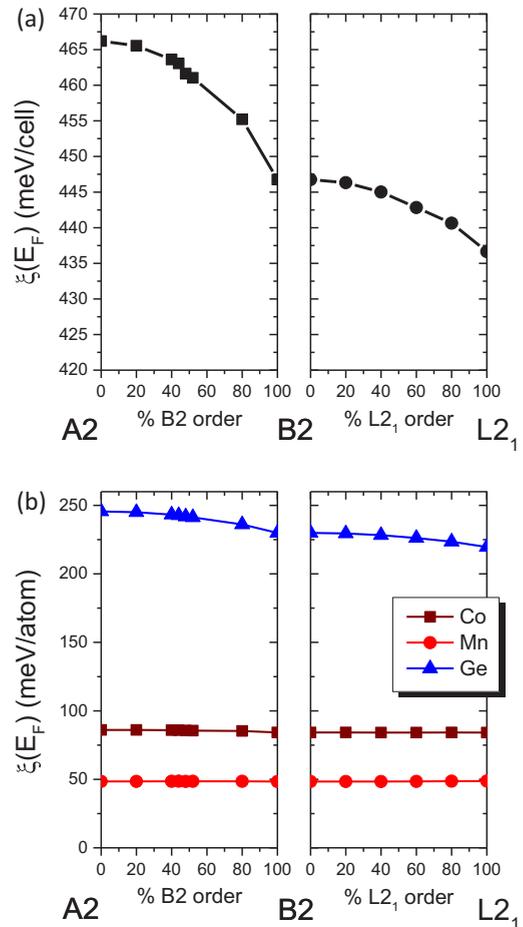
FIG. 10. (a) Composition weighted sum of the spin-orbit parameter for Co and Mn $3d$ orbitals and Ge $4p$ orbitals, for the unit cell of CMG, as a function of degree of ordering. (b) Element specific value of Co and Mn $3d$ as well as Ge $4p$ spin-orbit parameter for different ordering of CMG.

[29]. They report similar trends for the phases we considered for CMG in this work and discuss these results in the view of spin polarization and $n(E_F)$.

Another factor contributing to the damping is the strength of the spin-obit coupling (SOC). The effect of spin-orbit coupling on the damping has been analyzed by calculating the spin-orbit-splitting parameter $\xi \propto (\frac{1}{r})dV(r)/dr$ as a function of ordering, where $V(r)$ is the radial potential of the elements occupying different sublattices. Since the ordering does not affect the composition of CMG, we expect small changes in the spin-orbit-splitting parameter at the Fermi energy $\xi(E_F)$. Indeed, as Fig. 10(a) shows, $\xi(E_F)$, obtained as a concentration weighted sum of the spin-orbit splitting parameters of the $3d$ electrons of Co and Mn and the $4p$ electrons of Ge, is 466 meV per cell for $A2$ phase while it is 436 meV per cell in the $L2_1$ ordered state. However, this 6% change in $\xi(E_F)$ mostly occurs between ≈60% and 100% $B2$ order, yielding a value of 446 meV per cell for $B2$ ordered CMG. This small (≈6%), albeit noticeable change in the SOC is driven by the Ge $4p$ orbitals shown in Fig. 10(b), which illustrates the element-specific spin-orbit-splitting parameters in different states of ordering of CMG. These element-specific values are in good agreement

with previously reported values [75]. The trend in SOC is very similar to the trend of the calculated damping parameter, shown in Fig. 8(b), and the trend of the calculated g factor in Fig. 6(b). Since both the g factor and the damping parameter are governed by SOC, this trend might be expected. However, we note that other effects must play a significant role, because the modification of the spin-orbit parameter is rather small. As discussed, details of the electronic structure around the Fermi level play a decisive role.

In addition to the $n(E_F)$, additional band overlap that results from band broadening—due to atomic disorder, electron correlations, and thermal fluctuations—will increase the damping due to interband transitions [76]. In fact, our calculations indicate that the damping is dominated by such interband transitions. This particular contribution to the damping should therefore correlate to the resistivity of the material as previously calculated for CMG and Co_2MnSi [21]. Such an expected correlation is based on the assumption that the electron scattering time determines the spin scattering time that is responsible for spin relaxation. We therefore measured the resistivity of our films via a four-point probe method to compare with the damping of the films. The values for the damping are taken from the 16-nm films since they have minimal spin-pumping contributions. The resistivity of the CMG layer was separated from the seed and capping layers via the thickness dependence of the sheet resistance since the sheet resistance of the seed and capping layers will remain constant. Figure 11(a) shows that indeed the damping and resistivity of the films are well correlated. The change in resistivity is likely a result of structural disorder of the material, i.e., the resistivity is lower for samples with higher B2 order. The data in Fig. 11(a) are consistent with the interband scattering contribution to the damping being dominant, which was predicted from our calculations.

Thermal fluctuations should also contribute to band broadening from increased scattering. As a result, within the interband damping regime, both the damping and the resistivity should decrease as the temperature is reduced. Indeed, as Fig. 11(b) shows, there is a ≈30% reduction of the resistivity at 5 K versus 300 K for the 16 nm, 400 °C annealed sample. However, the damping parameter remains largely constant as a function of measurement temperature. At first glance, a comparison of the data in Figs. 11(a) and 11(b) suggests that the spin scattering is more strongly affected by structural disorder versus thermal fluctuations. However, the band structure and $n(E_F)$ are not constant as the structural disorder is varied by changing the annealing temperature. In contrast, the band structure and $n(E_F)$ are not expected to change considerably as the temperature is reduced from RT. As a result, we can conclude that the damping is dominated by $n(E_F)$ and the formation of a band gap in the minority band. This is further supported by calculations of the damping parameter at 10 K, which are included in Fig. 8(b). Here, there is little difference in the calculated damping parameter at 300 K versus 10 K. These data indicate that although the damping is dominated by interband transitions, thermal band broadening is not a major contributor to the band overlap, at least at RT or below.

Finally, it is important to point out that the measured values of resistivity in our films are rather high for CMG, which
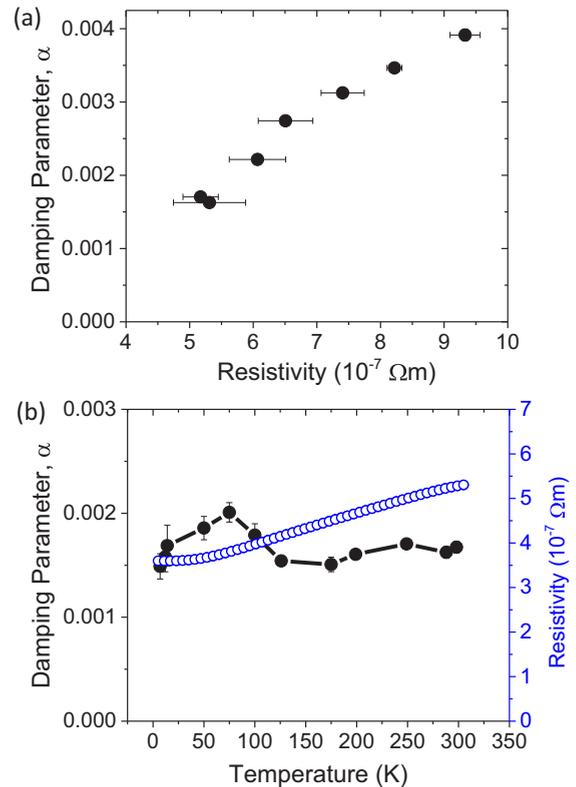
FIG. 11. (a) Damping parameter vs resistivity for samples annealed at different temperatures. (b) Damping parameter and resistivity of the 16-nm sample annealed at 400 °C as a function of measurement temperature from RT down to approximately 5 K.

indicates significant disorder from the microstructure and/or crystalline structure [77]. As a result, our data further suggest that continued improvements in the growth of sputtered CMG (i.e., increasing the structural order) may result in a material with an intrinsic damping below 0.0010. In addition, since APT indicated that the resulting films contain excess Co, it is conceivable that the damping parameter may also be lowered by further optimization of the stoichiometry. This is supported by studies in similar Co_2MnSi and $Co_2Mn(Ge,Ga)$ systems, which show that Co antisites (Co occupying Mn, Ge, Ga, or Si sites) can destroy the band gap in the minority band [78–80].

V. SUMMARY

In summary, we have shown that exceptionally low values of magnetic damping can be achieved in sputtered CMG, which requires only an anneal to 400 °C. In films less than 20 nm thick, no $L2_1$ order is present; however, B2 order is achieved and can be varied depending on the annealing temperature. As a result, the damping parameter is tunable between approximately 0.004 to 0.001 by varying the annealing temperature from 240 °C to 400 °C. DFT calculations also show that the damping parameter is predicted to vary from 0.0075 to 0.0005 as the order is varied between $A2$, $B2$, and $L2_1$. Considering both experiment and theory, we conclude that this variation of the damping is related to the formation of a band gap in the minority band, or at least a significant reduction of $n(E_F)$,

as the $B2$ order improves with only a minimal decrease of the damping with further $L2_1$ order. While the damping is also proportional to $\xi(E_F)$, our calculations show only a $\approx 6\%$ change of $\xi(E_F)$ with different amounts of crystalline order, indicating that the variation of the damping is not dominated by changes in SOC. Of importance to many applications is the very low value of inhomogeneous linewidth broadening that is also achieved in this material. These results show that imperfect, polycrystalline Co_2MnGe films with only $B2$ order are sufficient for many low-damping applications. This is especially an attractive material since the required annealing temperature is at most 400 °C for sputter deposited thin films.

[1] G. A. Prinz, Phys. Today **48**, 58 (1995).

[2] P. B. Visscher and S. Wang, IEEE Trans. Magn. **42**, 3198 (2006).

[3] S. Mangin, Y. Henry, D. Ravelosona, J. A. Katine, and E. E. Fullerton, Appl Phys Lett **94**, 012502 (2009).

[4] T. Brächer, F. Heussner, P. Pirro, T. Meyer, T. Fischer, M. Geilen, B. Heinz, B. Lägel, A. A. Serga, and B. Hillebrands, Sci. Rep. **6**, 38235 (2016).

[5] K. Wagner, A. Kákay, K. Schultheiss, A. Henschke, T. Sebastian, and H. Schultheiss, Nat. Nanotechnol. **11**, 432 (2016).

[6] V. V. Kruglyak, S. O. Demokritov, and D. Grundler, J. Phys. D: Appl. Phys. **43**, 264001 (2010).

[7] A. V. Chumak, V. I. Vasyuchka, A. A. Serga, and B. Hillebrands, Nat. Phys. **11**, 453 (2015).

[8] A. Khitun, J. Appl. Phys. **111**, 054307 (2012).

[9] M. Haertinger, C. H. Back, J. Lotze, M. Weiler, S. Geprägs, H. Huebl, S. T. B. Goennenwein, and G. Woltersdorf, Phys. Rev. B **92**, 054437 (2015).

[10] B. Heinrich, C. Burrowes, E. Montoya, B. Kardasz, E. Girt, Y. -Y. Song, Y. Sun, and M. Wu, Phys. Rev. Lett. **107**, 066604 (2011).

[11] H. Chang, P. Li, W. Zhang, T. Liu, A. Hoffmann, L. Deng, and M. Wu, IEEE Magn. Lett. **5**, 1 (2014).

[12] S. Fujii, S. Sugimura, Ishida, and S. Asano, J. Phys. Condens. Matter **2**, 8583 (1990).

[13] I. Galanakis, P. H. Dederichs, and N. Papanikolaou, Phys. Rev. B **66**, 174429 (2002).

[14] H. C. Kandpal, G. H. Fecher, and C. Felser, J. Phys. Appl. Phys. **40**, 1507 (2007).

[15] S. Trudel, O. Gaier, J. Hamrle, and B. Hillebrands, J. Phys. Appl. Phys. **43**, 193001 (2010).

[16] S. Andrieu, A. Neggache, T. Hauet, T. Devolder, A. Hallal, M. Chshiev, A. M. Bataille, P. Le Fèvre, and F. Bertran, Phys. Rev. B **93**, 094417 (2016).

[17] J. Ma, V. I. Hegde, K. Munira, Y. Xie, S. Keshavarz, D. T. Mildebrath, C. Wolverton, A. W. Ghosh, and W. H. Butler, Phys. Rev. B **95**, 024411 (2017).

[18] A. Rajanikanth, Y. K. Takahashi, and K. Hono, J. Appl. Phys. **101**, 023901 (2007).

[19] M. Zhu, B. D. Soe, R. D. McMichael, M. J. Carey, S. Maat, and J. R. Childress, Appl. Phys. Lett. **98**, 072510 (2011).

[20] T. Kubota, Y. Ina, Z. Wen, H. Narisawa, and K. Takanashi, Phys. Rev. Mater. **1**, 044402 (2017).

[21] C. Liu, C. K. A. Mewes, M. Chshiev, T. Mewes, and W. H. Butler, Appl. Phys. Lett. **95**, 022509 (2009).

[22] S. Lounis, M. dos Santos Dias, and B. Schweflinghaus, Phys. Rev. B **91**, 104420 (2015).

[23] J. Chico, S. Keshavarz, Y. Kvashnin, M. Pereiro, I. Di Marco, C. Etz, O. Eriksson, A. Bergman, and L. Bergqvist, Phys. Rev. B **93**, 214439 (2016).

[24] S. Mizukami, D. Watanabe, M. Oogane, Y. Ando, Y. Miura, M. Shirai, and T. Miyazaki, J. Appl. Phys. **105**, 07D306 (2009).

[25] P. Dürrenfeld, F. Gerhard, J. Chico, R. K. Dumas, M. Ranjbar, A. Bergman, L. Bergqvist, A. Delin, C. Gould, L. W. Molenkamp, and J. Åkerman, Phys. Rev. B **92**, 214424 (2015).

[26] C. Sterwerf, S. Paul, B. Khodadadi, M. Meinert, J. -M. Schmalhorst, M. Buchmeier, C. K. A. Mewes, T. Mewes, and G. Reiss, J. Appl. Phys. **120**, 083904 (2016).

[27] A. Köhler, L. Wollmann, D. Ebke, S. Chadov, C. Kaiser, Z. Diao, Y. Zheng, Q. Leng, and C. Felser, Phys. Rev. B **93**, 094410 (2016).

[28] S. Husain, S. Akansel, A. Kumar, P. Svedlindh, and S. Chaudhary, Sci. Rep. **6**, 28692 (2016).

[29] B. Pradines, R. Arras, I. Abdallah, N. Biziere, and L. Calmels, Phys. Rev. B **95**, 094425 (2017).

[30] S. He, Y. Liu, Y. Zheng, Q. Qin, Z. Wen, Q. Wu, Y. Yang, Y. Wang, Y. Feng, K. L. Teo, and C. Panagopoulos, Phys. Rev. Mater. **1**, 064401 (2017).

[31] T. Seki, H. Yako, T. Yamamoto, T. Kubota, Y. Sakuraba, M. Ueda, and K. Takanashi, J. Phys. Appl. Phys. **48**, 164010 (2015).

[32] T. Yamamoto, T. Seki, and K. Takanashi, Phys. Rev. B **94**, 094419 (2016).

[33] H. B. Huang, X. Q. Ma, Z. H. Liu, C. P. Zhao, and L. Q. Chen, AIP Adv. **3**, 032132 (2013).

[34] S. Mizukami, F. Wu, A. Sakuma, J. Walowski, D. Watanabe, T. Kubota, X. Zhang, H. Naganuma, M. Oogane, Y. Ando, and T. Miyazaki, Phys. Rev. Lett. **106**, 117201 (2011).

[35] T. Sebastian, Y. Ohdaira, T. Kubota, P. Pirro, T. Brächer, K. Vogt, A. A. Serga, H. Naganuma, M. Oogane, Y. Ando, and B. Hillebrands, Appl. Phys. Lett. **100**, 112402 (2012).

[36] J. R. Childress, M. J. Carey, S. Maat, N. Smith, R. E. Fontana, D. Druist, K. Carey, J. A. Katine, N. Robertson, T. D. Boone, M. Alex, J. Moore, and C. H. Tsang, IEEE Trans Magn **44**, 90 (2008).

[37] M. J. Carey, S. Maat, S. Chandrashekariaih, J. A. Katine, W. Chen, B. York, and J. R. Childress, J. Appl. Phys. **109**, 093912 (2011).

[38] M. J. Carey, T. Block, and B. A. Gurney, Appl. Phys. Lett. **85**, 4442 (2004).

[39] H. Lefakis, M. Benaissa, P. Humbert, V. S. Speriosu, J. Werckmann, and B. A. Gurney, J. Magn. Magn. Mater. **154**, 17 (1996).

[40] C. T. Boone, H. T. Nembach, J. M. Shaw, and T. J. Silva, J. Appl. Phys. **113**, 153906 (2013).

[41] J. M. Shaw, H. T. Nembach, M. Weiler, T. J. Silva, M. Schoen, J. Z. Sun, and D. C. Worledge, IEEE Magn. Lett. **6**, 1 (2015).

[42] M. A. W. Schoen, J. M. Shaw, H. T. Nembach, M. Weiler, and T. J. Silva, Phys. Rev. B **92**, 184417 (2015).

[43] M. Sparks, R. Loudon, and C. Kittel, Phys. Rev. **122**, 791 (1961).

[44] M. J. Hurben and C. E. Patton, J. Appl. Phys. **83**, 4344 (1998).

[45] J. Lindner, K. Lenz, E. Kosubek, K. Baberschke, D. Spoddig, R. Meckenstock, J. Pelzl, Z. Frait, and D. L. Mills, Phys. Rev. B **68**, 060102 (2003).

[46] J. Lindner, I. Barsukov, C. Raeder, C. Hassel, O. Posth, R. Meckenstock, P. Landeros, and D. L. Mills, Phys. Rev. B **80**, 224421 (2009).

[47] H. T. Nembach, T. J. Silva, J. M. Shaw, M. L. Schneider, M. J. Carey, S. Maat, and J. R. Childress, Phys. Rev. B **84**, 054424 (2011).

[48] J. M. Shaw, H. T. Nembach, T. J. Silva, and C. T. Boone, J. Appl. Phys. **114**, 243906 (2013).

[49] B. Heinrich, J. F. Cochran, and R. Hasegawa, J. Appl. Phys. **57**, 3690 (1985).

[50] M. Farle, Rep. Prog. Phys. **61**, 755 (1998).

[51] R. D. McMichael and P. Krivosik, IEEE Trans. Magn. **40**, 2 (2004).

[52] E. Schloemann, IEEE Trans. Magn. **28**, 3300 (1992).

[53] http://ebert.cup.uni-muenchen.de/sprkkr.

[54] H. Ebert, D. Ködderitzsch, and J. Minár, Rep. Prog. Phys. **74**, 096501 (2011).

[55] P. Soven, Phys. Rev. **156**, 809 (1967).

[56] G. M. Stocks, W. M. Temmerman, and B. L. Gyorffy, Phys. Rev. Lett. **41**, 339 (1978).

[57] S. H. Vosko, L. Wilk, and M. Nusair, Can. J. Phys. **58**, 1200 (1980).

[58] H. Ebert, S. Mankovsky, D. Ködderitzsch, and P. J. Kelly, Phys. Rev. Lett. **107**, 066603 (2011).

[59] H. Ebert, S. Mankovsky, K. Chadova, S. Polesya, J. Minár, and D. Ködderitzsch, Phys. Rev. B **91**, 165132 (2015).

[60] W. H. Butler, Phys. Rev. B **31**, 3260 (1985).

[61] M. Sargolzaei, M. Richter, K. Koepernik, I. Opahle, H. Eschrig, and I. Chaplygin, Phys. Rev. B **74**, 224410 (2006).

[62] T. Ishikawa, T. Marukame, K. Matsuda, T. Uemura, M. Arita, and M. Yamamoto, J. Appl. Phys. **99**, 08J110 (2006).

[63] K. Miyamoto, A. Kimura, K. Iori, K. Sakamoto, T. Xie, T. Moko, S. Qiao, M. Taniguchi, and K. Tsuchiya, J. Phys. Condens. Matter **16**, S5797 (2004).

[64] I. Galanakis, Phys. Rev. B **71**, 012413 (2005).

[65] V. Kambersky, B. Heinrich, and D. Fraitova, Phys. Lett. **23**, 26 (1966).

[66] V. Kambersky and C. E. Patton, Phys. Rev. B **11**, 2668 (1975).

[67] K. Gilmore, M. D. Stiles, J. Seib, D. Steiauf, and M. Fähnle, Phys. Rev. B **81**, 174414 (2010).

[68] T. Qu and R. H. Victora, J. Appl. Phys. **115**, 17C506 (2014).

[69] D. Thonig and J. Henk, New J. Phys. **16**, 013032 (2014).

[70] A. A. Starikov, P. J. Kelly, A. Brataas, Y. Tserkovnyak, and G. E. W. Bauer, Phys. Rev. Lett. **105**, 236601 (2010).

[71] S. Mankovsky, D. Ködderitzsch, G. Woltersdorf, and H. Ebert, Phys. Rev. B **87**, 014430 (2013).

[72] R. Mondal, M. Berritta, and P. M. Oppeneer, Phys. Rev. B **94**, 144419 (2016).

[73] M. A. W. Schoen, D. Thonig, M. L. Schneider, T. J. Silva, H. T. Nembach, O. Eriksson, O. Karis, and J. M. Shaw, Nat. Phys. **12**, 839 (2016).

[74] H. Lee, Y. -H. A. Wang, C. K. A. Mewes, W. H. Butler, T. Mewes, S. Maat, B. York, M. J. Carey, and J. R. Childress, Appl. Phys. Lett. **95**, 082502 (2009).

[75] A. R. Mackintosh and O. K. Andersen, *Electrons Fermi Surface: Condensed Matter Physics, Nanoscience and Mesoscopic Physics* (Cambridge University Press, 1980).

[76] K. Gilmore, Y. U. Idzerda, and M. D. Stiles, Phys. Rev. Lett. **99**, 027204 (2007).

[77] L. Ritchie, G. Xiao, Y. Ji, T. Y. Chen, C. L. Chien, M. Zhang, J. Chen, Z. Liu, G. Wu, and X. X. Zhang, Phys. Rev. B **68**, 104430 (2003).

[78] S. Picozzi, A. Continenza, and A. J. Freeman, Phys. Rev. B **69**, 094423 (2004).

[79] B. Hülsen, M. Scheffler, and P. Kratzer, Phys. Rev. B **79**, 094407 (2009).

[80] S. Li, Y. K. Takahashi, Y. Sakuraba, N. Tsuji, H. Tajiri, Y. Miura, J. Chen, T. Furubayashi, and K. Hono, Appl. Phys. Lett. **108**, 122404 (2016).